# Thermomechanical behavior and microstructural evolution of SiN$_x$/Al bimaterial microcantilevers

**I-Kuan Lin[1], Xin Zhang[1] and Yanhang Zhang[1,2,3]**

[1] Department of Mechanical Engineering, Boston University, Boston, MA 02215, USA
[2] Department of Biomedical Engineering, Boston University, Boston, MA 02215, USA

E-mail: yanhang@bu.edu

## Abstract

Bimaterial microcantilevers are used in numerous applications in microelectromechanical systems (MEMS) for thermal, mechanical, optical, tribological and biological functionalities. Unfortunately, the residual stress-induced curvature and combined effects of creep and stress relaxation in the thin film significantly compromises the performance of these structures. To fully understand the themomechanical deformation and microstructural evolution of such microcantilevers, SiN$_x$/Al bilayer cantilever beams were studied in this work. These microcantilevers were heated and subsequently cooled for five cycles between room temperature and 250 °C, with the peak temperature in each successive cycle increased in increments of 25 °C using a custom-built micro-heating stage. The *in situ* curvature change was monitored using an interferometric microscope. The general behavior of the bimaterial microcantilever beams can be characterized by linear thermoelastic regimes with $(\mathrm{d}\kappa/\mathrm{d}T)_{\mathrm{ave}} = 0.079$ mm$^{-1}$ °C$^{-1}$ and inelastic regimes. After thermal cycling with a maximum temperature of 225 °C, upon returning to room temperature, the bimaterial microcantilever beams were flattened and the curvature decreased by 99%. The thermoelastic deformation during thermal cycling was well described by the Kirchhoff plate theory. Deformation of bimaterial microcantilevers during long-term isothermal holding was studied at temperatures of 100 °C, 125 °C and 150 °C with a holding period of 70 h. The curvature of bimaterial microcantilever beams decreased more for higher holding temperatures. Finite element analysis (FEA) with power-law creep in Al was used to simulate the creep and stress relaxation and thus the curvature change of the bimaterial microcantilever beams. The microstructure evolutions due to isothermal holding in SiN$_x$/Al microcantilevers were studied using an atomic force microscope (AFM). The grain growth in both the vertical and lateral directions was present due to isothermal holding. As the isothermal holding temperature increased, the surface roughness of the film increased with more prominent grain structures.

(Some figures in this article are in colour only in the electronic version)

## 1. Introduction

Bilayer microcantilevers abound in MEMS applications, serving as both sensors and actuators such as microelectromechanical variable blaze gratings [1], infrared (IR) detectors [2], dc electrical relays and contacts [3], calorimetric high-frequency detectors [4], radio frequency (RF) components including switches [5] or variable capacitors [6], biological [7] or chemical [8] sensors and vertical [9] or lateral [10] actuators. Unfortunately, the manufacturability, planarity and reliability for such bilayer microcantilevers have been inadequate. The released bilayer microcantilevers always deflected due to the residue strain/stress in the bilayer system. To meet performance and reliability requirements, it is of the utmost

---

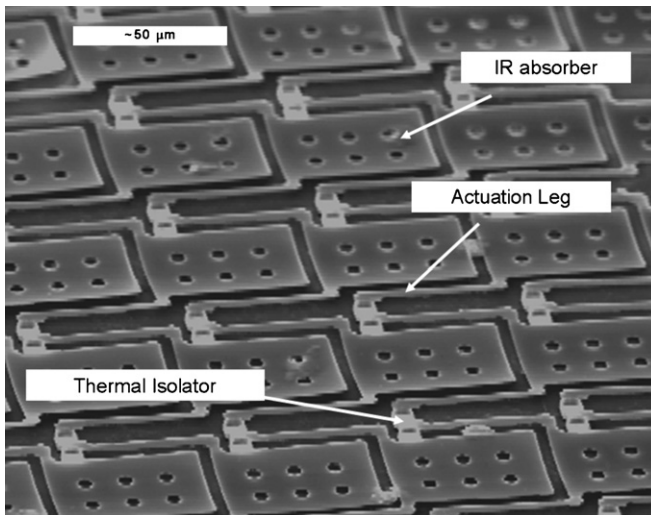[3] Author to whom any correspondence should be addressed.

**Figure 1.** SEM image of microcantilever-based IR FPAs. Each pixel consisted of (i) IR radiation absorber, (ii) actuation legs and (iii) thermal isolator.

importance to fully understand the thermomechanical behavior of bilayer microcantilevers, in order to better design, characterize and manufacture successful MEMS structures and devices for the next generation.

The importance of successful development of MEMS is clear to our community, which is also aware of the need for leading researchers in the field to identify promising new materials and structures for MEMS and to master and characterize technologies that will qualify these materials and structures for robust and reliable system applications. In this paper, we use uncooled microcantilever-based IR focal plane arrays (FPAs), which have recently gained interest due to their low noise equivalent temperature difference (NETD) and low cost [11–13], as a case study of understanding the fundamental thermomechanical deformation and microstructural evolution of bilayer microcantilevers. The function of this kind of IR detector is based on the bending of bimaterial microcantilevers upon absorption of IR radiation. Subsequently, the deformation can be readily determined by using piezoresistive, optical or capacitive methods [11–16]. The $SiN_x$/Al bimaterial microcantilevers are often chosen as the sensing element because $SiN_x$ is one of the most ideal IR absorbers for wavelengths ranging from 8 to 14 $\mu$m and there is a large mismatch between thermal expansion coefficients (CTE) of $SiN_x$ and Al [17, 18]. As shown in figure 1, each pixel of the microcantilever-based IR FPAs is comprised of a thin $SiN_x$ top layer deposited on a thin Al layer on the bottom. Note that thermal isolation is one of the important issues in IR application. In order to optimize the temperature rise of IR detectors, the thermal conduction between IR detectors and environment should be minimized by using narrow supporting structures and low conductance material such as $SiN_x$ [13, 19, 20]. However thermal isolation issue is not considered in this study. As described later, the microcantilevers were placed in a temperature chamber for uniform heating/cooling.

Aside from microcantilever-based IR detectors, bilayer microcantilevers possess multiple practical roles and applications in MEMS [21]. The introduction of bilayer systems exhibits an aspect of ambivalence; while it establishes a degree of design freedom, it also admits unique material behavior and reliability issues. It is important to point out the two critical problems, which could greatly compromise the performance and functionality of the bilayer microcantilevers-based devices. First, the as-fabricated microcantilevers curve because of the imbalanced residual stresses, which developed during fabrication for reasons such as the presence of impurities or voids, grain growth and recrystallization [22]. Therefore, residual stress measurement [23, 24] and curvature modification [18, 25, 26] are the important topics in the post-process assessment of microcantilever-based devices. Second, for many applications, it is crucial to accurately control the deformation of bilayer microcantilevers over a significant period of time in order to meet performance and reliability requirements [27]. This is especially important for bilayer microcantilever-based detectors that are subjected to thermal loading. The combined effects of creep and stress relaxation in the metal layer significantly influence deformation and compromise device performance, therefore these effects must be fully understood.

To this end, we designed microcantilever $SiN_x$/Al bilayer beams to study the thermomechanical deformation and microstructural evolution for MEMS applications such as infrared detectors [11–16]. The goal of this study is to integrate the results from thermomechanical and material studies to improve the manufacturability, planarity and reliability of bilayer microcantilevers. Section 2 describes the fabrication of bimaterial microcantilever beams, which consist of 200 nm $SiN_x$ and 200 nm Al using a low-temperature surface micromachining technique with a commercial polyimide as the sacrificial layer. After the fabrication, the deflection of microcantilever beams subjected to thermal cycling and isothermal holding were *in situ* measured using interferometric microscopy. In section 3, finite element analysis (FEA) was used to present the thermomechanical deformation during thermal cycling and isothermal holding. Section 4 describes the thermomechanical evolution and the modeling during thermal cycling. Also discussed here is the use of AFM to study the microstructural evolution during isothermal holdings.

## 2. Experiment

### 2.1. Bimaterial microcantilever beams fabrication

Arrays of bimaterial microcantilever beams were fabricated using surface micromachining with polyimide as the sacrificial layer. Figure 2 shows the released $SiN_x$/Al bimaterial microcantilever beams. Each array consisted of five cantilever beams of 20 $\mu$m in width, and 40–120 $\mu$m in length with 20 $\mu$m increments. These microcantilever beams, consisting of 200 nm of Al as the bottom layer and 200 nm of $SiN_x$ as the top layer. To acquire maximum thermomechanical deformation, the thickness of both layers in the bimaterial microcantilever could be optimized [14, 28, 29].

The ⟨1 0 0⟩ silicon wafer was first cleaned with 40% hydrofluoric acid solution (HF) to strip off the native oxides
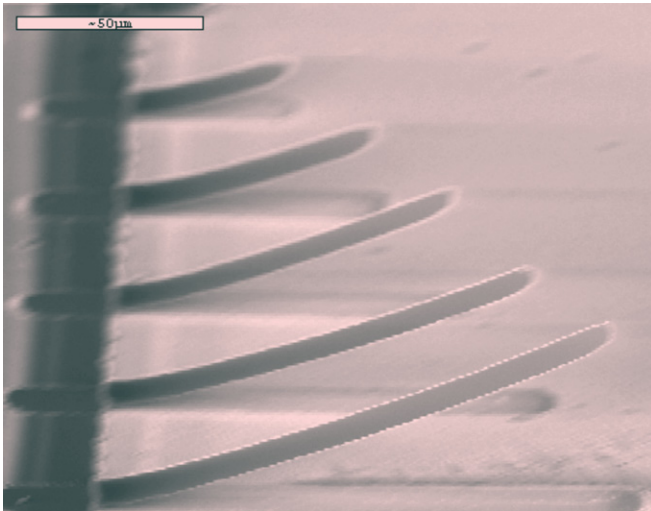
**Figure 2.** SEM image of an array of bimaterial SiN$_x$ (200 nm)/Al (200 nm) microcantilevers.



**Figure 3.** Fabrication process flow of SiN$_x$/Al bimaterial microcantilevers.



**Figure 4.** *In situ* deformation measurement setup consists of (*a*) WYKO interferometric microscope, (*b*) thermal system and (*c*) control system.

from its surface. The initial step in the fabrication process is to deposit a 2.5 $\mu$m thick polyimide layer, which acts as a sacrificial layer. The use of commercial PI 2610 polyimide (HD Microelectronics) not only allows for an all-dry final structure release step that overcomes stiction problems, but also completes compatibility with deposition and patterning of bimaterial structural layers, i.e., plasma-enhanced chemical vapor deposited (PECVD) SiN$_x$ and e-beam evaporated Al [25, 28, 30]. An adhesion promoter VM-652 was coated on silicon wafers at 3000 rpm for 30 s to enhance adhesion between polyimide and the wafer, and was baked at 90 °C for 10 min. The polyimide layer was spun on at 2200 rpm for 30 s, and then cured in a convention oven for 10 min at 150 °C with a nitrogen atmosphere as shown in figure 3(*a*) [31]. To create anchors of the microcantilever beams, an etching process was performed on the sacrificial layer. A SiO$_x$ layer of 500 nm was deposited on the top of the sacrificial layer as a hard mask using PECCD and patterned by reactive ion etching (RIE) with gases SF$_6$ and He [32]. The anchor holes on the polyimide layer were fabricated using RIE with O$_2$ plasma as shown in figure 3(*b*). After RIE etching, the SiO$_x$ layer was removed by using the buffered oxide etcher (BOE) because it does not have an effect on polyimide. Following the etching processes, SiN$_x$ and Al layers were deposited on the top of the polyimide. The process began with a deposition of a 200 nm layer Al using an E-beam thermal evaporator, followed by PECVD of a 200 nm SiN$_x$ layer on the top of the Al, as shown in figure 3(*c*). The SiN$_x$ and Al layers were patterned using RIE with SF$_6$ and He, and phosphoric acid, respectively [32]. Finally, the SiN$_x$/Al microcantilever beams were released by removing the polyimide sacrificial layer using isotropic O$_2$ plasma dry etching as shown in figure 3(*d*).

## 2.2. Measurement procedure

The *in situ* deformation of microcantilever beams was measured using an interferometer microscope and a thermal system as shown in figure 4. The microcantilever beams were
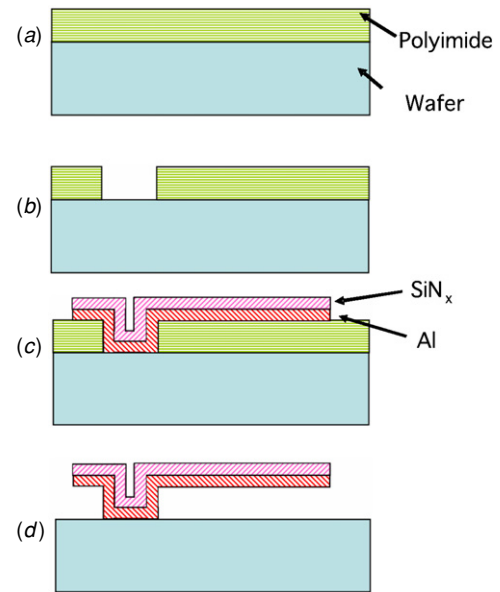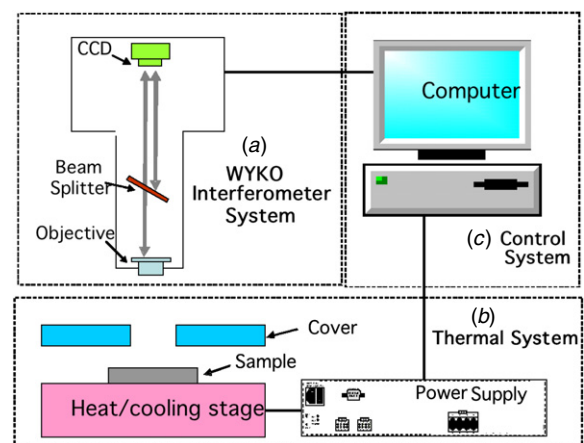
subjected to a controlled temperature change using a thermal system consisting of a custom-made heating/cooling stage and a close-loop heating and cooling controller with 0.1 °C resolution [33]. Simultaneously, a visual representation of the full-field out-of-plane deformation, $w(x,y)$, of microcantilever beams with 100 nm resolution was archived (figure 5(*a*)) when a beam of white light passed through a 10× microscope objective to the surface of the microcantilever. Subsequently, an interferometer beam splitter reflects half of the incidence beam to the reference surface inside the microscope. These two beams are recombined and projected onto the camera to generate a signal that is proportional to the resultant beam intensity produced by the interference effect. These signals are then transferred into the spatial frequency domain and the surface height for each point is obtained from the complex phase as a function of the frequency [34]. From the full-field out-of-plane deformation (figure 5(*a*)), we determined the
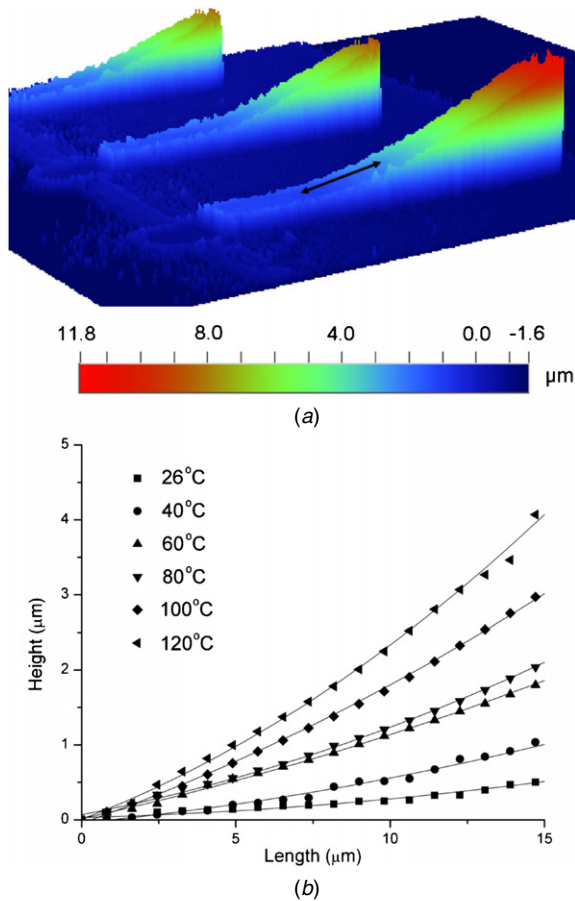
**Figure 5.** (*a*) Three-dimensional image of the as-fabricated microcantilever beams measured using the interferometer and (*b*) surface profiles of beam at different temperatures along the arrow line in (*a*).

curvature along the length of the microcantilever beam (the *x*-direction) by fitting $w(x,y)$ with a second-order polynomial and then differentiating as appropriate; typical results are shown in figure 5(*b*). Using the thermal system to heat/cool the microcantilever beams, we can measure the curvature evolution *in situ* as shown in figure 5(*b*) [35]. For example, the series of surface profiles of the microcantilever beam show that the deformation increased with increasing temperature as the Al expands more than the $SiN_x$ layer. This measurement setup provided a suitable representation for the overall thermomechanical response using calculated curvatures at each temperature.

In this study, in order to characterize the thermomechanical behavior of the microcantilever beams, thermal cycling and isothermal holding experiments were performed. The test protocol was designed to carefully study the deformation of the $SiN_x$/Al microcantilever beams upon release, and then upon subsequent uniform heating, cooling and holding. The two tests proceed as follows:

*Thermal cycling:*

The thermal cycling procedure was designed to carefully explore the deformation of the microcantilever beams due to uniform heating and cooling cycles. In the first cycle, the microcantilever beams were heated from room temperature

to 150 °C at a rate of about 200 °C min$^{-1}$. When the microcantilever beams' temperature approached the target temperature, the heating rate decreased to about 10 °C min$^{-1}$ as the temperature slowly approached the target temperature. The cooling rate upon cooling from the peak temperature is about the same as the heating rate. During the heating and cooling processes, the full-field deformation was measured using an interferometric microscope at increments of 20 °C. The temperature was held constant for 3 min to maintain the equilibrium at each increment. After the first thermal cycle, the microcantilevers were heated and subsequently cooled for four more cycles with 175 °C, 200 °C, 225 °C and 250 °C as the peak temperatures.

*Isothermal holding:*

In order to study the effects of creep and stress relaxation at different holding temperatures (100 °C, 125 °C and 150 °C), we measured the deformation of the microcantilevers as a function of time. First, the microcantilever beams were thermal cycled three times between room temperature and the holding temperatures to partially stabilize the Al microstructure. After the initial three thermal cycles, the microcantilever beams were held at the isothermal holding temperature for about 70 h. The full-field out of plane deformation was measured during the initial three thermal cycles and the isothermal holding period.

## 3. Finite element modeling

Finite element modeling of the thermoelastic response and inelastic deformation of the microcantilever beams during isothermal holding were carried out using ABAQUS. In the simulations, the beam was meshed with composite shell elements to approximate the thin-plate kinematics of the Kirchhoff theory [36]. The microcantilever beam was fixed at one of the two ends and the parameters of geometry conformed to real structures. Residual stress in each layer was not considered in the model. The input parameters of the finite element model are shown in table 1 [37]. For the thermoelastic response simulation, the mismatch strain was induced in the bimaterial structures due to the thermal expansion mismatch between Al and $SiN_x$ and uniform temperature change. This mismatch strain will consequently result in bending curvature of the bimaterial structure [38]. For inelastic deformation simulation during isothermal holding, we modeled the curvature evolution as a function of time by assuming the inelastic deformation mechanism described by power-law creep in Al, $\dot{\varepsilon} = A\sigma^n$, and that the $SiN_x$ layer deforms elastically. Within ABAQUS, the power-law creep is implemented in a standard formalism through the Mises stress potential [39]. The power-law parameters, *A* and *n*, were obtained by fitting model results to the experimental data for the beams.

## 4. Results and discussion

### 4.1. Thermal cycling

The microcantilever-based IR FPAs function thermomechanically and the initial curvature observed in the structures is

**Table 1.** Material parameters used in the finite element model.

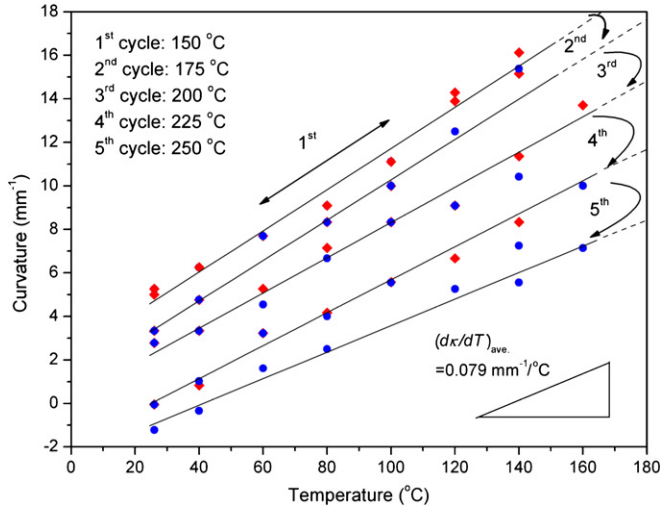|        | Young's modulus | Poisson's ratio | CTE | Thickness |
|--------|-----------------|-----------------|-----|-----------|
| SiN$_x$ | 254 Gpa | 0.2 | $2.1 \times 10^{-6}$ K$^{-1}$ | 200 nm |
| Al | 70 Gpa | 0.3 | $23 \times 10^{-6}$ K$^{-1}$ | 200 nm |



**Figure 6.** Curvature versus temperature for bimaterial SiN$_x$ (200 nm)/Al (200 nm) microcantilever beams during the five thermal cycles with different peak temperatures. The diamond and circle symbols are measured curvature during heating and cooling processes in each cycle, respectively.

very similar to that observed in those used in this study [25]. Figure 6 shows the *in situ* measurement of curvature versus temperature for the bilayer SiN$_x$/Al microcantilever beam including both linear thermoelastic and inelastic regimes. Results, measured with the interferometer microscope, show that the as-released microcantilever beams bent up due to the residual stress in the two layers [40]. When the temperature is increased, the curvature of beams also increases as the CTE of Al is higher than that of SiN$_x$. It is an inherent characteristic of microcantilevers that the misfit strains in the film layers lead to stresses in the layers and deformation of the structure upon temperature change. In figure 6, the measured curvature evolution is linearly dependent on temperature change between room temperature and 160 °C, indicating a linear thermoelastic deformation of microcantilever beams in this temperature region. However the full-field deformation measurement cannot be obtained at high temperatures, since the beams curve so much that the reflected light cannot be collected by the objective lens.

In the first cycle, while the temperature is increased towards the peak temperature of 150 °C, the curvature also increases with a constant rate of d$\kappa$/d$T$. Upon cooling, the sample exhibits a linear thermoelastic mechanical response with d$\kappa$/d$T$ that is approximately equal to the heating response. During the second cycle, the curvature also increases as the temperature is increased. Upon cooling, as d$\kappa$/d$T$ remains about the same as heating, there is a shift of the linear thermoelastic mechanical behavior. This indicates that during heating between 160 °C and the peak temperature of 175 °C,

the sample experiences inelastic deformation that is manifested by nonlinear stress–strain relationships. After returning to room temperature, the curvature drops form 5.1 mm$^{-1}$ to 3.2 mm$^{-1}$. These results indicate the release of residue stress/strain in the microcantilevers during thermal cycling. The deformation behaviors during the following cycles are similar, exhibiting thermoelastic responses upon heating until a nonlinear behavior start. The cooling process is again thermoelastic with the subsequent room temperature curvature decreasing after each cycle. Furthermore, after the fourth cycle with a peak temperature of 225 °C, upon return to room temperature the microcantilever beam bends down toward the substrate and the curvature is about −0.05 mm$^{-1}$. Hence, optimized peak temperature of thermal cycling for flattening the SiN$_x$/Al microcantilevers beams should be very close to but less then 225 °C. Thermal cycling treatment with optimized peak temperature could be obtained to fully flatten the microcantilevers beams.

From our measurements, thermal cycling appears to be an effective method to modify the residual stress-induced curvature. We also have previously studied the thermal mechanisms of microcantilever-based IR detectors and have reduced the curvature via thermal cycling [25]. Similar phenomena have also been observed by Zhang and Dunn [38] on the curvature evolution of Au/polysilicon bilayer microcantilevers. The average curvature $\kappa$ of microcantilever beams depends on the mismatch strain $\Delta\alpha\Delta T$, where $\Delta\alpha$ is the CTE mismatch of bimaterial structures and $\Delta T$ is the temperature change, and can be expressed as [38, 41]

$$\kappa = \frac{6\Delta\alpha T}{t_2}hm\left[\frac{1+h}{1+2hm\left(2+3h+2h^2\right)+h^4m^2}\right], \quad (1)$$

where $h = t_1/t_2$ and represents the thickness ratio, $m = M_1/M_2$ (where $M_i = E_i/1 - \nu_i$) is the Young's modulus ratio and the subscripts 1 and 2 denote the SiN$_x$ and Al of bimaterial structures, respectively. In figure 6, the average d$\kappa$/d$T$ from five cycles is 0.079 mm$^{-1}$ °C$^{-1}$ and it agrees with the analytical solution (0.074 mm$^{-1}$ °C$^{-1}$) from equation (1) with material properties listed in table 1.

In our previous study [25], we observed the thermo-mechanical response of bimaterial SiN$_x$/Al microcantilever-based IR detectors using thermal cycling. However, equation (1) cannot model the thermoelastic response of microcantilever-based IR detectors, mainly due to the relatively complex geometry and boundary conditions of the detector structures. We thus modified the analytical solution based in plate theory by using a correction factor derived from FEA.

### 4.2. Isothermal holding

Figure 7 shows the curvature evolution as a function of temperature between room temperature and 125 °C for bimaterial SiN$_x$/Al microcantilever beams during three pre-thermal cycles and isothermal holding. The response shows the three regimes of deformation: (i) during the three pre-thermal cycles, the deformation is thermoelastic with a constant d$\kappa$/d$T$. After the three thermal cycles, the temperature
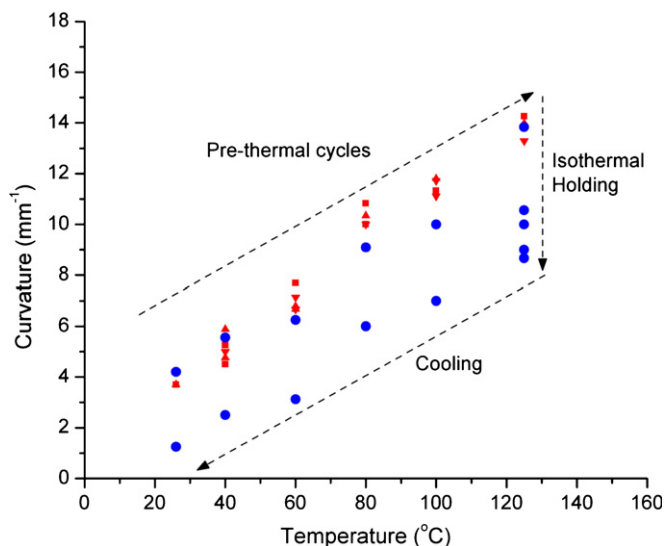
**Figure 7.** Curvature evolution during the pre-thermal cycles, isothermal holding and subsequent cooling to room temperature.



**Figure 8.** Measured and predicted curvature development during the 70 h of isothermal holding at 100, 120 and 150 °C for bilayer $SiN_x$/Al microcantilever beams. The symbols represent experimental data while the solid lines represent predictions.

was again increased from room temperature to 125 °C, and held for about 70 h. (ii) During the 70 h of isothermal holding, the deformation is inelastic and the curvature decreases due to the combined effects of creep and stress relaxation. (iii) Upon cooling from 125 °C, the deformation is again thermoelastic with the same $d\kappa/dT$ as seen in the pre-thermal cycles. When the temperature reaches room temperature, the curvature is lower than the initial room temperature curvature due to the inelastic deformation during isothermal holding [39, 42–46].

Figure 8 shows the curvature development during the isothermal hold at 100, 120, 150 °C for bilayer $SiN_x$/Al microcantilever beams. The symbols represent experimental data while the solid lines represent finite element predictions. During the isothermal holding, the curvature of the $SiN_x$/Al microcantilever beams significantly decreases due to the combined effects of creep and stress relaxation. Both stress and strain are not constant during the isothermal holding. Higher holding temperature triggers more creep and stress relaxation in the Al film, which is manifested by more prominent decrease in the curvature. After the isothermal holding at 100 °C, 125 °C and 150 °C, the curvature decreases by 8%, 37% and 66% of the initial curvature, respectively. The curvature decreases more rapidly over the first 20 h, which is consistent with the results from previous studies that stress relaxation is most pronounced during the early stages of the isothermal holding [39, 47].

Power-law creep was used to describe the inelastic deformation behavior of $SiN_x$/Al microcantilever beams during isothermal holding. With a constant $n = 5$ and different $A$ values ($A = 8 \times 10^{-15}$ h$^{-1}$ MPa$^{-5}$, $1 \times 10^{13}$ h$^{-1}$ MPa$^{-5}$ and $3 \times 10^{-12}$ h$^{-1}$ MPa$^{-5}$ for 100 °C, 125 °C and 150 °C), the inelastic behavior during isothermal holding are well described. While these parameters were chosen to fit the data, they are in reasonable agreement with thin film data in the literature as described earlier [45, 47]. Power-law creep has been used to describe the inelastic deformation behavior of thin Al film on thick Si substrate [47] and
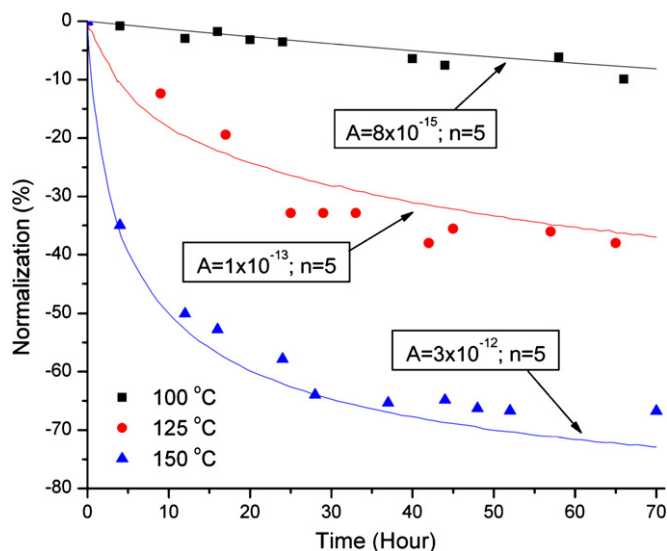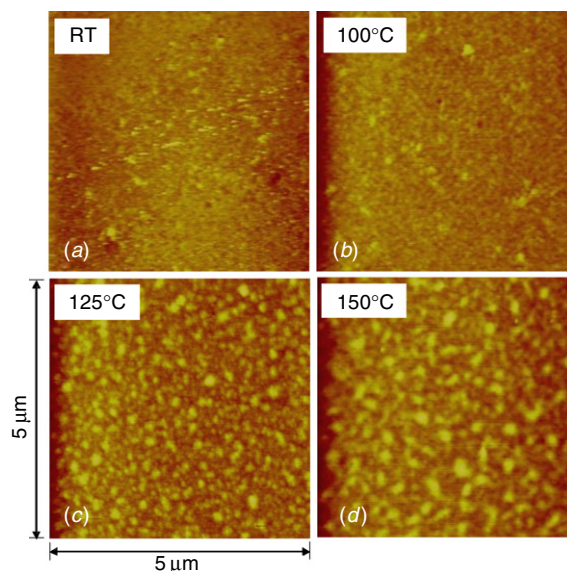


**Figure 9.** A series of AFM top-view images showing the grain growth on Al surface (*a*) before, and after 70 h isothermal holding at (*b*) 100 °C, (*c*) 125 °C and (*d*) 150 °C.

Au/polysilicon bilayer microcantilever structures [39]. The value of $A$ has been shown to depend on the film thickness and holding temperatures [39, 45]. Nonlinear deformation mechanisms associated with microstructural changes in the bimaterial microstructures are of contemporary interest and will be discussed in section 4.3.

### 4.3. Microstructural evolution

It is of great interest to understand the mechanisms of microstructural evolution on a more local scale during the deformation and stress relaxation of $SiN_x$/Al bimaterial microcantilevers. The Al surface morphology was measured
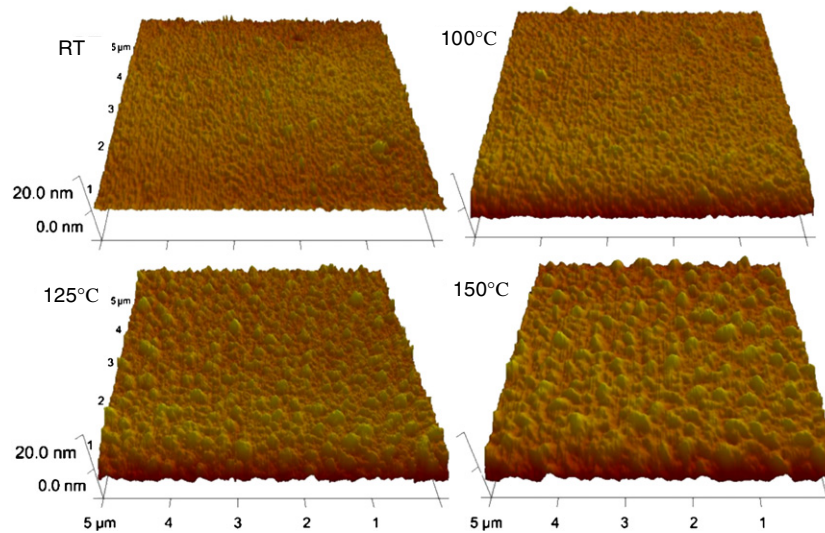
**Figure 10.** A series of AFM 3D images showing the grain growth on Al surface (*a*) before, and after 70 h isothermal holding at (*b*) 100 °C, (*c*) 125 °C and (*d*) 150 °C.

using an AFM on both the as-released and thermally treated microcantilevers. In order to measure the surface morphology of the Al layer located at the bottom of the structure, the microcantilevers were separated from the sample substrates by placing carbon adhesive tapes on the top of the samples. Figures 9 and 10 show the morphology of the Al layer of bimaterial microcantilever beams with the effect of various isothermal holdings. Initially, the Al surface of the as-released microcantilever beams at room temperature had a fairly smooth surface as shown in figures 9(*a*) and 10(*a*). Figures 9(*b*) and 10(*b*) show surface morphology of the Al surfaces after isothermal holding at 100 °C. The morphology of Al surfaces is not significantly different compared with the as-released microcantilever beams. After isothermal holdings at higher temperatures of 125 °C and 150 °C, however, the small grain coalesce to produce a big grain and morphology measurement shows the surface of Al layer are rougher, as seen in figures 9(*c*)–(*d*) and 10(*c*)–(*d*), respectively. The mean roughness ($R_a$) and mean square roughness ($R_q$) of the Al layer of microcantilever beams are shown in table 2. The roughness of the Al surface is increased by 4.6%, 47.6% and 50.8% compared to the as-released structures after isothermal holdings at 100 °C, 125 °C and 150 °C, respectively.

Similar results were found in previous studies of isothermal anneals of thin Al or Al alloy films on thick substrates [48–51]. Volkert *et al* showed the grain growth of pure Al from 0.15 $\mu$m to 0.6 $\mu$m after cycling the sample to 500 °C [49]. Iwamura *et al* measured that the grain size of Al–Ta alloy change from 0.06 $\mu$m to 0.1 and 0.21 $\mu$m after annealing at 533 K for 14.4 ks and 673 K for 3.6 ks, respectively [50]. The morphology changes and compressive stress relief for isothermal annealing has been well documented in an effort to better understand the stress-induced reliability problem in microelectronic interconnects. However the results from our study using thin Al films on a substrate of comparable thickness, show the morphology changes and the grain growths associated with the thermomechanical deformation of bimaterial microcantilevers for MEMS applications.

Compressive stress in metal thin films is relaxed by various mechanisms, such as grain growth and hillock formation. The normal boundary migration leads to grain growth, which generates a tensile stress in the plane of the film when the initial grain size is below a critical size [50]. When the grain size reaches a particular value, the sum of the strain energy and surface energy is minimized. Further grain growth can continue if plastic flow releases the strain energy [24, 48]. When the grain size is over a critical size, infinite grain size is produced by boundary migration such as hillocks [52]. Hillock formation is the other main factor that tends to happen at higher temperature or longer holding time. The hillock size is typically a few microns and could increase with increasing annealing temperature. The distance between each hillock ranged from 20 $\mu$m to 100 $\mu$m. The hillocks relieve stress within a small vicinity, while grain growth and stress relaxation dominate elsewhere [50]. In our study, the grain growth is the main factor in morphology change of Al surface, as observed in figures 9 and 10. Similar results can be seen in previous research on Au/Si cantilever beams [53]. Grain growth was observed after 100 h at 180 °C and the hillock formation after 200 h at 180 °C. The hillock formation also occurred under a compressive stress due to the diffusion of Al atoms along the grain boundaries and the film surface [51]. Grain growth can homogeneously change the microstructure of Al film but the hillock formation non-homogeneously changes the microstructure of Al.

To better understand the microstructure evolution during isothermal holding, stress development through the thickness of the bilayer microcantilevers was plotted in figure 11 for $t = 0, 5, 25$ and 70 h. To eliminate the edge effect, the stress is plotted at the center of the beam. The thickness from 0 to 0.2 $\mu$m is in the Al layer, and from 0.2 to 0.4 $\mu$m is in the SiN$_x$ layer. At $t = 0$ stress gradient exists across both the Al and SiN$_x$ layers. During the first 5 h of isothermal holding the stresses in both Al and SiN$_x$ layers decrease and redistribute significantly. After 25 h of isothermal holding,
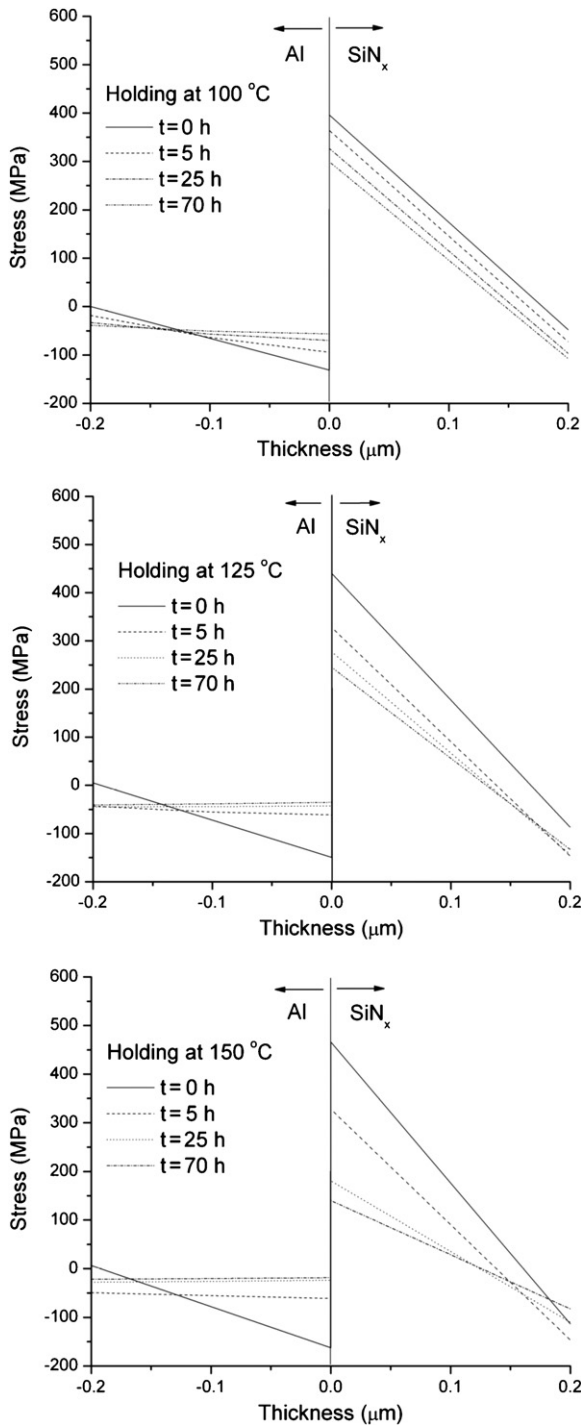
**Figure 11.** Stress destitutions in both Al and SiN$_x$ layers of bimaterial microcantilever beams at 0, 5, 25, and 70 h of isothermal holding at (*a*) 100 °C, (*b*) 125 °C and (*c*) 150 °C.

**Table 2.** Roughness measured on the surface the Al layer of the bimaterial microcantilever beams.

|  | 23 °C | 100 °C | 125 °C | 150 °C |
|---|---|---|---|---|
| $R_a$ (nm) | 0.65 | 0.68 | 0.96 | 0.98 |
| $R_q$ (nm) | 0.85 | 0.89 | 1.23 | 1.41 |

microstructural grain growth associated with creep and stress relaxation during isothermal holding.

## 5. Conclusion

In this paper, SiN$_x$/Al bimaterial microcantilevers were fabricated using surface micromachining with a sacrificial polyimide layer. A thermal system and an interferometric microscope were used to *in situ* measure the full-field out-of-plane deformation of microcantilever beams. The deformation mechanisms with different thermal loading, including thermal cycling and isothermal holding were studied. Thermal cycling appears to be an effective method to modify the residual stress-induced curvature. Combined effects of creep and stress relaxation can greatly compromise the device performance, and can be simulated with power-law creep in Al to predict the curvature changes of the bimaterial microcantilevers. Moreover, morphology changes and grain growth of the Al surface were well captured using AFM, and was associated with the thermomechanical behavior and stress development of bimaterial microcantilevers. We would like to emphasize that the scope of this paper is not at all limited by IR detectors, which is only a specific application that could potentially benefit from this research. The scientific insights from this study contribute to the fundamental understanding of many other similar bilayer thin film material systems commonly used in MEMS. Broadly speaking, this paper would also help to identify more effective means for engaging the materials science and engineering mechanics community in work important to continuing advances in MEMS technology.

## References

[1] Burns D M and Bright V M 1998 Development of microelectromechanical variable blaze gratings *Sensors Actuators* A **64** 7–15
[2] Senesac L R, Corbeil J L, Rajic S, Lavrik N V and Datskos P G 2003 IR imaging using uncooled microcantilever detectors *Ultramicroscopy* **97** 451–8

stresses distribute almost constantly through the thickness of the Al layer and change slowly for the rest of the holding period. From figure 11 we can see that the isothermal holding conducted at higher temperature results in more compressive stress relief, which may trigger the small grains to coalesce with each other to form a bigger grain. These results on stress distribution, combined with the surface morphology measurement in figures 9 and 10, help us better understand

[3] Miller D C, Zhang W G and Bright V M 2001
Micromachined, flip-chip assembled, actuatable contacts
for use in high density interconnection in electronics
packaging *Sensors Actuators* A **89** 76–87

[4] Lee S, Wallis T M, Moreland J, Kabos P and Lee Y C 2007
Asymmetric dielectric trilayer cantilever probe for
calorimetric high-frequency field imaging *J.
Microelectromech. Syst.* **16** 78–86

[5] Chang C L and Chang P Z 2000 Innovative micromachined
microwave switch with very low insertion loss *Sensors
Actuators* A **79** 71–5

[6] Bell P, Hoivik N, Bright V and Popovic Z 2003 A frequency
tunable half-wave resonator using a MEMS variable
capacitor *Microelectron. Int.* **20** 21–5

[7] Raiteri R, Grattarola M, Butt H J and Skladal P 2001
Micromechanical cantilever-based biosensors *Sensors
Actuators* B **79** 115–26

[8] Baselt D R, Fruhberger B, Klaassen E, Cemalovic S, Britton
C L, Patel S V, Mlsna T E, McCorkle D and Warmack B
2003 Design and performance of a microcantilever-based
hydrogen sensor *Sensors Actuators* B **88** 120–31

[9] Riethmuller W and Benecke W 1988 Thermally excited silicon
microactuators *IEEE Trans. Electron Devices*
**35** 758–63

[10] Dai C L, Yen K S and Chang P Z 2001 Applied electrostatic
parallelogram actuators for microwave switches using the
standard CMOS process *J. Micromech. Microeng.*
**11** 697–702

[11] Amantea R, Goodman L A, Pantuso F, Sauer D J, Varghese M,
Villani T S and White L K 1998 Progress towards an
uncooled IR imager with 5 mK NETD *Proc. SPIE*
**3436** 647–59

[12] Grbovic D, Lavrik N V, Datskos P G, Forrai D, Nelson E,
Devitt J and McIntyre B 2006 Uncooled infrared imaging
using bimaterial microcantilever arrays *Appl. Phys. Lett.*
**89** 073118

[13] Zhao Y, Mao M Y, Horowitz R, Majumdar A, Varesi J, Norton
P and Kitching J 2002 Optomechanical uncooled infrared
imaging system: design, microfabrication, and performance
*J. Microelectromech. Syst.* **11** 136–46

[14] Miao Z Y, Zhang Q C, Chen D P, Guo Z Y, Dong F L, Xiong
Z M, Wu X P, Li C B and Jiao B B 2007 Uncooled IR
imaging using optomechanical detectors *Ultramicroscopy*
**107** 610–6

[15] Datskos P G, Lavrik N V and Rajic S 2004 Performance of
uncooled microcantilever thermal detectors *Rev. Sci.
Instrum.* **75** 1134–48

[16] Hunter S R, Maurer G, Jiang L and Simelgor G 2006
High-sensitivity uncooled microcantilever infrared imaging
arrays *Proc. SPIE* **6206** 62061J

[17] Li B 2004 Design and simulation of an uncooled
double-cantilever microbolometer with the potential for
similar to mK NETD *Sensors Actuators* A **112** 351–9

[18] Huang S S, Li B and Zhang X 2006 Elimination of
stress-induced curvature in microcantilever infrared focal
plane arrays *Sensors Actuators* A **130** 331–9

[19] Rogalski A 2003 Infrared detectors: status and trends *Prog.
Quantum Electron.* **27** 59–210

[20] Dong F L, Zhang Q C, Chen D P, Pan L, Guo Z Y, Wang W B,
Duan Z H and Wu X P 2007 An uncooled optically readable
infrared imaging detector *Sensors Actuators* A
**133** 236–42

[21] Gall K, Dunn M L, Zhang Y H and Corff B A 2004 Thermal
cycling response of layered gold/polysilicon MEMS
structures *Mech. Mater.* **36** 45–55

[22] Zhang X, Chen K S, Ghodssi R, Ayon A A and Spearing S M
2001 Residual stress and fracture in thick
tetraethylorthosilicate (TEOS) and silane-based PECVD
oxide films *Sensors Actuators* A **91** 373–80

[23] Lu J 1996 *Handbook of Measurement of Residual Stresses*
(Lilburn, GA: Fairmount Press)

[24] Chen K S, Chen T Y F, Chuang C C and Lin I K 2004
Full-field wafer level thin film stress measurement by
phase-stepping shadow Moire *IEEE Trans. Compon.
Packag. Technol.* **27** 594–601

[25] Lin I K, Zhang Y H and Zhang X 2008 The deformation of
microcantilever-based infrared detectors during thermal
cycling *J. Micromech. Microeng.* **18** 075012

[26] Bifano T G, Johnson H T, Bierden P and Mali R K 2002
Elimination of stress-induced curvature in thin-film
structures *J. Micromech. Microeng.* **11** 592–7

[27] Miller D C, Dunn M L and Bright V M 2001 Thermally
induced change in deformation of multimorph MEMS
structures *Proc. SPIE* **4558** 32–44

[28] Huang S, Tao H, Lin I K and Zhang X 2008 Development of
double-cantilever infrared detectors: Fabrication, curvature
control and demonstration of thermal detection *Sensors
Actuators* A **145** 231–40

[29] Lai J, Perazzo T, Shi Z and Majumdar A 1997 Optimization
and performance of high-resolution micro-optomechanical
thermal sensors *Sensors Actuators* A **58** 113–9

[30] Bagolini A, Pakula L, Scholtes T L M, Pham H T M, French
P J and Sarro P M 2002 Polyimide sacrificial layer and
novel materials for post-processing surface micromachining
*J. Micromech. Microeng.* **12** 385–9

[31] HD Microsystems Inc 2000 PI2620 Data Sheet

[32] Williams K R, Gupta K and Wasilik M 2003 Etch rates for
micromachining processing: II *J. Microelectromech. Syst*
**12** 761–78

[33] Instec Inc HCP302-STC200 Data Sheet

[34] Degroot P and Deck L 1993 3-dimensional imaging by
sub-Nyquist sampling of white-light interferograms *Opt.
Lett.* **18** 1462–4

[35] Dunn M L, Zhang Y H and Bright V M 2002 Deformation and
structural stability of layered plate microstructures
subjected to thermal loading *J. Microelectromech. Syst.*
**11** 372–84

[36] Hibbit, Karlsson & Sorensen, Inc 1998 ABAQUS User Manual

[37] Shackelford J F and Alexander W 2001 *CRC materials
Science and Engineering Handbook* (Sound Parkway, NW:
CRC Press)

[38] Zhang Y H and Dunn M L 2003 Deformation of blanketed and
patterned bilayer thin-film microstructures during
post-release and cyclic thermal loading *J.
Microelectromech. Syst.* **12** 788–96

[39] Zhang Y H and Dunn M L 2004 Geometric and material
nonlinearity during the deformation of micron-scale
thin-film bilayers subject to thermal loading *J. Mech. Phys.
Solids* **52** 2101–26

[40] Vinci R P and Vlassak J J 1996 Mechanical behavior of thin
films *Ann. Rev. Mater. Sci.* **26** 431–62

[41] Freund L B, Floro J A and Chason E 1999 Extensions of the
Stoney formula for substrate curvature to configurations
with thin substrates or large deformations *Appl. Phys. Lett.*
**74** 1987–9

[42] Weiss D, Gao H and Arzt E 2001 Constrained diffusional
creep in UHV-produced copper thin films *Acta Mater.*
**49** 2395–403

[43] Baker S P, Kretschmann A and Arzt E 2001
Thermomechanical behavior of different texture
components in Cu thin films *Acta Mater.*
**49** 2145–60

[44] Leung O S, Munkholm A, Brennan S and Nix W D 2000 A
search for strain gradients in gold thin films on substrates
using x-ray diffraction *J. Appl. Phys.* **88** 1389–96

[45] Keller R M, Baker S P and Arzt E 1999 Stress-temperature
behavior of unpassivated thin copper films *Acta Mater.*
**47** 415–26

[46] Vickers-Kirby D J, Kubena R L, Stratton F P, Joyce R J, Chang D T and Kim J 2000 Anelastic creep phenomena in thin metal plated cantilevers for MEMS *Mater. Res. Soc. Symp.* **657** EE2.5.1–EE2.5.6

[47] Shen Y L and Suresh S 1995 Thermal cycling and stress-relaxation response of Si-Al and Si-Al-Sio$_2$ layered thin-films *Acta Metall. Mater.* **43** 3915–26

[48] Chaudhari P 1972 Grain growth and stress relief in thin films *J. Vac. Sci. Technol.* **9** 520–2

[49] Volkert C A, Alofs C F and Liefting J R 1994 Deformation mechanisms of Al films on oxidized Si wafers *J. Mater. Res.* **9** 1147–55

[50] Iwamura E, Ohnishi T and Yoshikawa K 1995 A study of hillock formation on Al-Ta alloy films for interconnections of TFT-LCDs *Thin Solid Films* **270** 450–5

[51] Onishi T, Iwamura E and Takagi K 1999 Morphology of sputter deposited Al alloy films *Thin Solid Films* **340** 306–16

[52] Hwang S J, Lee Y D, Park Y B, Lee J H, Jeong C O and Joo Y C 2006 In situ study of stress relaxation mechanisms of pure Al thin films during isothermal annealing *Scr. Mater.* **54** 1841–6

[53] Gall K, West N, Spark K, Dunn M L and Finch D S 2004 Creep of thin film Au on bimaterial Au/Si microcantilevers *Acta Mater.* **52** 2133–46